Journal of Building Engineering 80 (2023) 108097

Contents lists available at ScienceDirect

Journal of Building Engineering

journal homepage: www.elsevier.com/locate/jobe

Full length article

Numerical simulation of CLT moisture uptake and dry-out following water infiltration through end-grain surfaces

Florian Brandstätter [a,*], Kristo Kalbe [b], Maximilian Autengruber [a], Markus Lukacevic [a], Targo Kalamees [b], Aime Ruus [c], Alvar Annuk [c], Josef Füssl [a]

[a] Institute for Mechanics of Materials and Structures, TU Wien, Karlsplatz 13, Vienna 1040, Austria
[b] NZEB Research Group, Department of Civil Engineering and Architecture, Tallinn University of Technology, Ehitajate Tee 5, 19086, Tallinn, Estonia
[c] Tartu College, Tallinn University of Technology, Puiestee 78, 51008, Tartu, Estonia

ARTICLE INFO

Keywords:
Coupled moisture transport
Heat mass transfer
Free water
CLT
Moisture uptake
Dry-out
Wood

ABSTRACT

Cross-laminated timber (CLT) offers the potential to construct advanced load-bearing walls and floors made of wood, as its larger dimensions and homogenized material properties expands the application possibilities. As for wood in general, CLT can be negatively affected by moisture. End-grain wetting of CLT coupled with conditions that trap moisture can be particularly problematic due to hindered drying. However, CLT end-grain wetting and subsequent moisture dry-out are hardly investigated and conventional models have not been able to simulate these conditions sufficiently. Here, we show that the moisture uptake and dry-out under this unfavorable condition can be realistically simulated using a moisture transport model including free water. We modeled a basic configuration of one-week wetting, followed by two weeks of dry-out in different climatic conditions. To refine the simulations, the mass transfer coefficients of water vapor and free water were calibrated. In a sensitivity analysis, the influence of both coefficients on moisture development was investigated, revealing that the most significant effect on moisture changes originates from the mass transfer coefficient of free water. Furthermore, the influence of glue lines connecting the layers of CLT panels on moisture transport was examined. The results suggest that the glue line has a minor influence on the moisture behavior of CLT surface layers, but the effects increase towards the middle layer.

1. Introduction

In addition to its numerous environmentally friendly properties, such as a lower environmental impact compared to other building materials like concrete, masonry and steel [1], wood offers several other advantages for constructional purposes. Construction time can be lower compared to concrete and steel buildings of equivalent size, and it has a remarkable strength-to-weight ratio. Moreover, when appropriately treated and designed, timber constructions can endure over 100 years [1], with the wood type influencing the structural elements' service life [2]. The use of engineered wood products, such as cross-laminated timber (CLT) instead of sawn timber, paves the way for constructing load-bearing walls and floors, as its larger dimensions and homogenized material properties expand the application possibilities of wood. Furthermore, buildings made of CLT typically demonstrate superior energy savings than comparable concrete structures [3]. Malle and Espinoza [4] illustrate cost saving potential when using structures

* Corresponding author.
E-mail address: florian.brandstaetter@tuwien.ac.at (F. Brandstätter).

https://doi.org/10.1016/j.jobe.2023.108097
Received 26 May 2023; Received in revised form 3 November 2023; Accepted 6 November 2023
Available online 7 November 2023

Nomenclature

CLT	cross-laminated timber
EMC	equilibrium moisture content
FSP	fiber saturation point
MAE	mean absolute error
MC	moisture content
RH	relative humidity
RMSE	root mean square error
c_b	bound water concentration ($kg\,m^{-3}$)
c_v	water vapor concentration ($kg\,m^{-3}$)
$c_{v,0}$	surrounding water vapor concentration ($kg\,m^{-3}$)
$c_{v_{sat}}$	saturated water vapor concentration ($kg\,m^{-3}$)
c_w	free water concentration ($kg\,m^{-3}$)
$c_{w,0}$	surrounding free water concentration ($kg\,m^{-3}$)
$\dot{c}_{bv}$	sorption rate of bound water and water vapor ($kg\,m^{-3}\,s^{-1}$)
$\dot{c}_{wb}$	sorption rate of free water and bound water ($kg\,m^{-3}\,s^{-1}$)
$\dot{c}_{wv}$	evaporation/condensation rate of free water and water vapor ($kg\,m^{-3}\,s^{-1}$)
$\mathbf{D_{air}}$	diffusion tensor of water vapor ($m^2\,s^{-1}$)
$\boldsymbol{f}$	heat flux ($W\,m^{-1}\,K^{-1}$)
f_{lum}	volume fraction of the lumen (–)
$f_{lum_{gas}}$	volume fraction of gaseous part of the lumen (–)
h_b	enthalpy of bound water ($J\,kg^{-1}$)
h_v	enthalpy of water vapor ($J\,kg^{-1}$)
h_w	enthalpy of water ($J\,kg^{-1}$)
$\bar{h}_b$	average enthalpy of bound water ($J\,kg^{-1}$)
$\mathbf{J_b}$	bound water flux ($kg\,m^2\,s^{-1}$)
$\mathbf{J_v}$	water vapor flux ($kg\,m^2\,s^{-1}$)
$\mathbf{J_w}$	free water flux ($kg\,m^2\,s^{-1}$)
$\boldsymbol{K_r}$	relative permeability tensor (–)
$\boldsymbol{K_w}$	absolute permeability tensor (m^2)
k_{c_v}	mass transfer coefficient for water vapor ($m\,s^{-1}$)
k_{c_w}	mass transfer coefficient for free water ($m\,s^{-1}$)
$k_{c_{v,d,\mathrm{in}}}$	mass transfer coefficient for water vapor during the drying phase in indoor climate conditions ($m\,s^{-1}$)
$k_{c_{v,d,\mathrm{out}}}$	mass transfer coefficient for water vapor during the drying phase in outdoor climate conditions ($m\,s^{-1}$)
$k_{c_{v,w}}$	mass transfer coefficient for water vapor during the wetting phase ($m\,s^{-1}$)
k_T	heat transfer coefficient for water vapor ($W\,m^{-2}\,K^{-1}$)
P_c	capillary pressure (Pa)
P_g	gas pressure (Pa)
T	temperature (K)
T_0	surrounding temperature (K)
t	time (s)
μ_w	dynamic viscosity of water (Pa s)
ρ_d	density of dry wood ($kg\,m^{-3}$)
ρ_{H_2O}	density of water ($kg\,m^{-3}$)
ϕ_T	boundary heat flux ($W\,m^{-2}$)
ϕ_v	boundary flux of water vapor ($kg\,m^{-2}\,s^{-1}$)
ϕ_w	boundary flux of free water ($kg\,m^{-2}\,s^{-1}$)

made of CLT instead of concrete, and Lu et al. [5] show that life cycle costs of laminated veneer lumber can be lower compared to concrete and steel, respectively, making CLT an excellent alternative to conventional building materials.

However, moisture can profoundly impair wood, reducing material properties such as strength [6] and stiffness [7]. Fluctuations in the ambient climate lead to moisture gradients, inducing stresses that may cause cracking [8,9]. In addition, durability is compromised by, e.g., decay and mold growth, which not only destroy the wooden structure but can also trigger health concerns

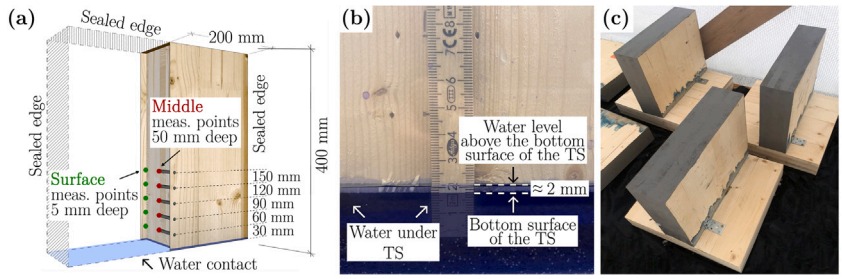

Fig. 1. Test specimens (TS) treatment scheme and measurement point layout (a). TS submersed approximately 2 mm into water (b) and TS during the drying phase in the outdoor shelter (c) [19].

like allergic reactions [10]. Mold growth depends on factors such as relative humidity (RH) and temperature levels, substrate as well as the duration and variability of these conditions [11].

These problems can also arise in CLT structures, as, e.g., shown by Austigard and Mattson [12], who examined fungi damage in eleven massive timber element buildings. The mold genera identified by the authors, primarily caused by moisture intrusion during the construction phase and constructional error, respectively, exhibited increased resistant to low temperatures, which could be a reason why mold can occur during the construction phases of cold months. To date, most scientists have focused on moisture-related issues for floors, walls and roofs [12–18], but the end-grain wetting and the resulting problems have received less attention. Kalbe et al. [19] investigated the vertical moisture uptake of six CLT structures during the construction phase, discovering high moisture content (MC) levels ($\geq$ 25%) in the CLT end-grain due to moisture intrusion during the installation and construction phase. Moisture trapping conditions occurred often, resulting in high MC levels for a long time, which led to damage like delamination and mold growth. To reduce the MC levels and avoid these problems, air dryers as well as heating were used. However, the dry climate caused moisture-induced stresses, leading to surface cracks in the CLT panels. Schmidt et al. [20] studied the geometrical and physical properties of a CLT floor panel subjected to wetting and drying cycles in an environmental chamber. The team highlighted that end-grain surfaces are problematic zones of CLT panels, especially in conditions where moisture dry-out is inhibited, increasing the chances of moisture-related damage. In addition, the moisture load led to swelling and restricted shrinkage in transverse direction, causing moisture-induced stresses, which resulted in cupping, checking, interfacial shearing, and possibly delamination.

To gain deeper insights into the moisture behavior of CLT end-grain surfaces, this work aims to replicate the experiments of Kalbe et al. [19] based on a numerical model including free water transport of Autengruber et al. [21]. The model was adapted to simulate a more sophisticated problem — to describe moisture transport considering all three characteristic directions of wood in one simulation. In Section 3.1, the results of the simulations for all investigated climates (indoor and outdoor) and storage conditions (exposure to air or another CLT panel) are presented. In order to simulate the MC evolution, parameter calibrations were necessary. The influence of these parameters on the MC change is introduced in Section 3.2, and the effect of the used adhesive in the CLT element is shown in Section 3.3. At last, Section 4 gives a conclusion and an outlook.

2. Materials and methods

2.1. Experiments

The experiment consisted of two parts: initially, a water uptake test of one week (wetting phase) and then a moisture dry-out test over the course of two weeks under four different climatic conditions (drying phase).

Twelve test specimens (TS) measuring 400 mm in length and 400 mm in height were cut from a five-layer CLT panel with a layer thickness of 20 mm each. The TS were made of spruce with an average dry density ρ_d of 415 kg m^{-3}. The TS were prepared largely in accordance with the European standard EN ISO 15148 [22] for determining the water absorption coefficient of a building material by partial immersion. However, unlike the standard preparation method, where only the surface immersed into water is left untreated and all other surfaces are coated with a water- and vapor-tight sealant, the side faces of the TS were left open in order to analyze the moisture dry-out through the corresponding faces. Three end-grain surfaces of the TS were covered with a liquid plastic coating (IKO MS Detail; see Fig. 1 (a)). The same TS were used throughout the entire experiment in both the wetting and drying phase. For a better visual illustration of the water uptake, blue ink (Parker Quink) was added to the water. Parker Quink has been deemed suitable for staining fungal structures in mycological studies [23] and does not alter the water uptake process. In addition, electrical resistance-based moisture measurements were performed to analyze the moisture distribution inside the TS. The results from the resistance-based moisture measurements were used in this work to validate the simulation model.

The TS were conditioned in sheltered outdoor climate conditions ($T \approx$ 275.15 K, RH $\approx$ 90%) for two weeks before the wetting phase. Although the TS were not exposed to free water at this stage, the surfaces of the TS absorbed water vapor from the surrounding air. This led to an elevated initial MC of up to 20% close to the surface of the TS. However, the internal layers remained at about 10% to 12% MC. More details about the initial conditions of the TS are given in conjunction with the description of the initial conditions for the simulation model in Section 2.2.1.

Table 1
Test conditions during the wetting and drying phase. Temperature (T) and relative humidity (RH) were measured with a Hobo UX100-023 data logger with its external sensor about 0.5 m from the test specimens (TS); SD = standard deviation.

	Indoor conditions, $T \approx 294.75$ K (SD = 0.8 K), RH ≈ 29% (SD = 5%)	Outdoor conditions, $T \approx 275.25$ K (SD = 2.7 K), RH ≈ 92% (SD = 5%)
Wet surface exposed to air	Group A (3 TS)	Group B (3 TS)
Wet surface against another CLT	Group C (3 TS)	Group D (3 TS)

At the beginning of the wetting phase, the TS were placed in containers where the water level was continuously controlled and kept at about 1 mm to 2 mm above the bottom surface of the TS (see Fig. 1 (b)). The TS were held in place by blunt pins, maximizing the water contact and reducing possible surface effects at the contact plane. The untreated bottom end-grain surfaces of the TS were in continuous water contact for one week. The experimental setup imitated a CLT wall panel, which would had its bottom surface subjected to free water during the construction phase and moisture dry-out would have been possible only through the side faces.

For the two-week drying phase, the twelve TS were divided into four groups with distinct conditions: indoor and outdoor climate with both uninhibited dry-out and moisture trapping conditions (see Table 1). The moisture trapping conditions were produced by fixing the TS onto another CLT plate, which imitated a CLT wall-to-floor connection (see Fig. 1 (c)). During the drying phase, none of the TS got into contact with free water.

There was a good drying potential in the indoor climate conditions (water vapor pressure difference between the surrounding air and the wet surfaces of the TS was about 1800 Pa), but the outdoor conditions provided only a marginal drying potential (≈ 50 Pa water vapor pressure difference). The ambient air temperature and RH data measured throughout the experiment for each climate condition are shown in Fig. 4 (a) in Section 2.4, where the moisture load conditions for the simulations are presented.

The electrical resistance-based MC measurements were made according to EN 13183–2 [24] with a Logica Holzmeister LG9 NG wood moisture meter (expanded uncertainty 0.8% for MC values between 12% and 22%) with 60 mm Teflon insulated pins which had 10 mm uninsulated peaks. MC was measured at two depths from the side faces (5 mm and 50 mm) and at five heights (30 mm, 60 mm, 90 mm, 120 mm, and 150 mm) from the bottom surface (see Fig. 1 (a)). The 5 mm deep measurements describe MC in the surface layer of the CLT and the 50 mm deep measurements describe conditions in the middle (3rd) layer of the 5-layer CLT. The wood grain direction was the same in both layers, with the bottom end-grain surface exposed to free water. The electrode pins for the surface and middle layer measurements were rammed in from the TS's opposite sides and perpendicular to the measured layer's wood grain. MC measurements were performed daily throughout the experiment. The results of the experiments have been previously discussed in [19,25]. The MC development at 120 mm and 150 mm, both in a depth of 5 mm and 50 mm, varied minimally, and therefore, only the results from the 30 mm, 60 mm and 90 mm height levels were taken from the experimental data for the validation of the simulation model (see Fig. 2).

2.2. Mathematical model for moisture transport in wood

To describe moisture transport including free water, the model of Autengruber et al. [21] is used, which is based on the multi-Fickian theory [26–31] for bound water and water vapor diffusion processes below the fiber saturation point (FSP) as well as on Darcy's law for free water transport (above the FSP). Besides, as introduced in Krabbenhoft et al. [32] and adopted by Autengruber et al. [21], a concentration-based formulation for free water flow in longitudinal direction is used. While bound water diffusion occurs in the cell wall, water vapor diffuses through the lumen, with the sorption rate coupling both processes. Similar to water vapor, free water is also assumed to be present only in the lumen, which is believed to occur exclusively above the FSP. The transition between bound and free water is defined by a sorption rate, while the interaction between water vapor and free water is described by an evaporation/condensation rate. The driving force within Darcy's law is the gradient of the difference between gaseous and capillary pressure. Furthermore, based on an energy conservation equation, thermal conduction processes and enthalpy changes are considered, where the latter is caused by phase change and transport processes. To describe these mechanisms, the following governing equations are used, where the three states of water are defined as concentrations (bound water concentration c_b, water vapor concentration c_v, and free water concentration c_w):

Conservation of bound water concentration:

$$\frac{\partial c_b}{\partial t} = -\frac{\partial}{\partial \boldsymbol{x}} \cdot \boldsymbol{J_b} + \dot{c}_{bv} + \dot{c}_{wb} \tag{1}$$

Conservation of water vapor concentration:

$$\frac{\partial c_v f_{lum_{gas}}}{\partial t} = -\frac{\partial}{\partial \boldsymbol{x}} \cdot \boldsymbol{J_v} f_{lum_{gas}} - \dot{c}_{bv} + \dot{c}_{wv} \tag{2}$$

Conservation of free water concentration:

$$\frac{\partial c_w}{\partial t} = -\frac{\partial}{\partial \boldsymbol{x}} \cdot \boldsymbol{J_w} - \dot{c}_{wb} - \dot{c}_{wv} \tag{3}$$

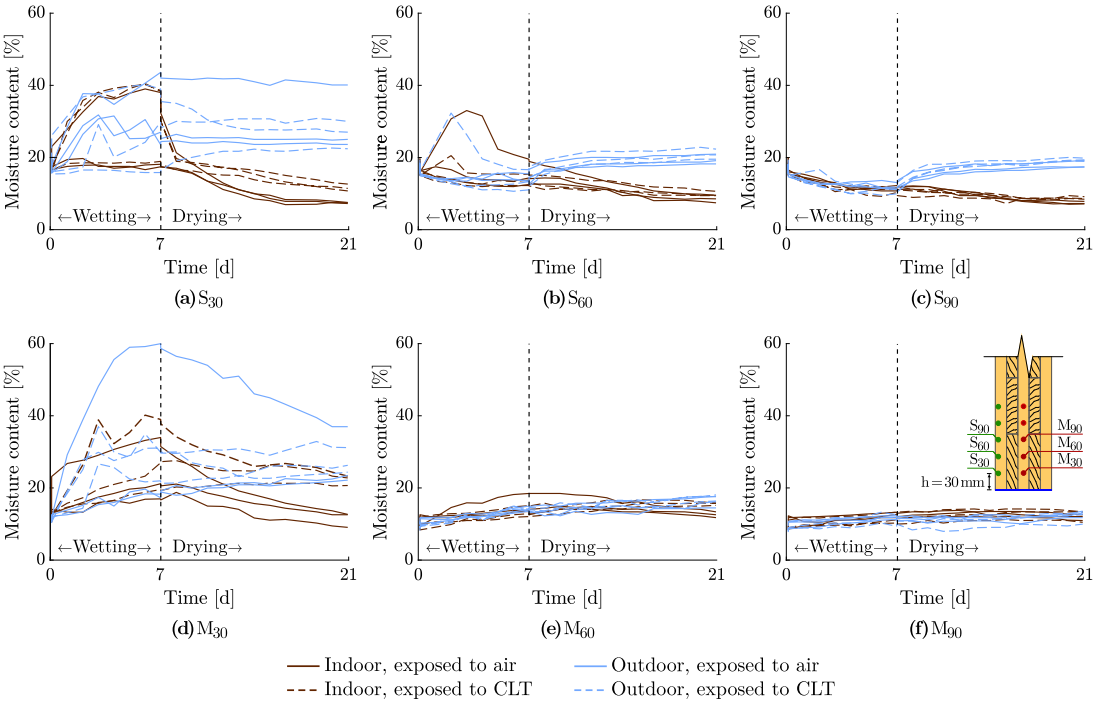

Fig. 2. Development of the measured moisture content (MC) of CLT during the wetting phase (0–7 days) and the drying phase (7–21 days). Measurements were taken (a, b, c) at a depth of 5 mm (S_i: surface measurement points at a height of i mm), and (d, e, f) at a depth of 50 mm (M_i: measurement points located in the middle layer at a height of i mm).

Conservation of energy:

$$\frac{\partial \rho\, h}{\partial t} = -\frac{\partial}{\partial \boldsymbol{x}} \cdot \boldsymbol{f} - \frac{\partial}{\partial \boldsymbol{x}} \cdot \boldsymbol{J_b}\, \overline{h}_b - \frac{\partial}{\partial \boldsymbol{x}} \cdot \boldsymbol{J_v}\, h_v\, f_{lum_{gas}} - \frac{\partial}{\partial \boldsymbol{x}} \cdot \boldsymbol{J_w}\, h_w + \dot{c}_{bv}\,(h_v - h_b) + \dot{c}_{wb}\,(h_w - h_b) + \dot{c}_{wv}\,(h_w - h_v) \tag{4}$$

The terms on the left-hand sides of the Eqs. (1) to (4) account for the change of concentration/energy over time ∂t. While c_b and c_w are related to the whole volume of the representative volume element (RVE), c_v is only referred to the lumen filled with gas, defined as the volume proportion $f_{lum_{gas}}$. $\boldsymbol{J_b}$, $\boldsymbol{J_v}$, and $\boldsymbol{J_w}$ describe the fluxes of bound water, water vapor, and free water and $\boldsymbol{f}$ denotes the heat flux. The sorption rates $\dot{c}_{bv}$ from bound water to water vapor and $\dot{c}_{wb}$ from free water to bound water along with the evaporation/condensation rate $\dot{c}_{wv}$ between free water and water vapor couple the conservations of the three water states. While $\overline{h}_b$ defines the averaged enthalpy of bound water, h_b is the specific enthalpy of bound water. h_v and h_w describe the specific enthalpies of water vapor and free water, respectively [21].

For free water flow in longitudinal direction, $\boldsymbol{J_w}$ is defined as

$$\boldsymbol{J_{w_L}} = -\rho_{H_2O}\; 39.2 \cdot 10^{-9} \exp(0.011 \cdot c_w)\, \frac{\partial c_w}{\partial \boldsymbol{x}} \tag{5}$$

whereas free water flow in radial and tangential direction reads:

$$\boldsymbol{J_{w_{R,T}}} = -\rho_{H_2O}\, \frac{\boldsymbol{K_r} \cdot \boldsymbol{K_w}}{\mu_w} \cdot \frac{\partial P_g - P_c}{\partial \boldsymbol{x}} \tag{6}$$

with ρ_{H_2O} as the density of water in $\mathrm{kg\,m^{-3}}$. $\boldsymbol{K_r}$ and $\boldsymbol{K_w}$ are the relative and absolute permeability, respectively, and μ_w describes the dynamic viscosity of water. P_g and P_c define the gaseous and the capillary pressure, respectively [21].

These differential equations were implemented in the commercial finite element software `Abaqus` [33] through a user element subroutine. Brick-type elements with linear interpolation functions were used for the discretization.

Due to changing temperature levels, a temperature-dependent sorption isotherm to determine the equilibrium moisture content EMC was used [34,35]:

$$\mathrm{EMC} = 0.01 \left(\frac{-T\, \ln(1 - RH)}{0.13 \left(1 - \left(\frac{T}{647.1} \right)^{-6.46} \right)} \right)^{1/(110\,T^{-0.75})} \tag{7}$$

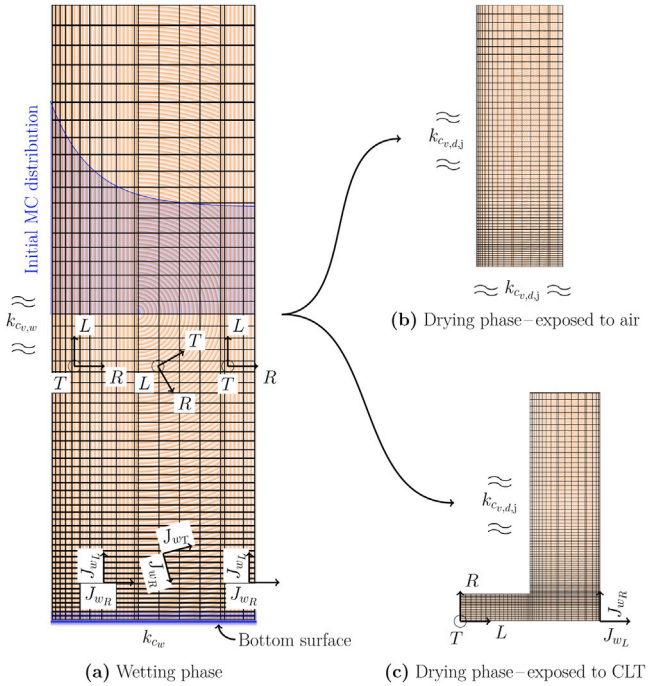

Fig. 3. Illustration of the models and parameters used for the wetting phase (a) (0–7 days) and the following drying phase (b) and (c), respectively (7–21 days). In (b), the bottom surface, which was in contact with water, is exposed to air, and in (c), the bottom surface is placed onto another CLT panel. In addition, each CLT layer's local coordinate system with the corresponding fiber orientations, including the related free water flow directions J_{w_i}, is displayed. Furthermore, the initial MC distribution is shown. The displayed mass transfer coefficients of water vapor $k_{c_{v,w}}$, $k_{c_{v,d,\mathrm{in}}}$ and $k_{c_{v,d,\mathrm{out}}}$ (see Eq. (10)) consider the related climate conditions during wetting and drying, respectively, (j = in, out; in = indoor and out = outdoor) at the left and bottom surfaces. k_{c_w} is the mass transfer coefficient of free water (see Eq. (8)).

2.2.1. Initial conditions

The initial conditions are based on the experimental data of Kalbe et al. [19], which are characterized by different initial MC values at the surface and middle layer measurement points (see Fig. 2) due to conditioning in sheltered outdoor climate conditions. To consider these non-uniform initial conditions, the initial water vapor concentration $c_{v,ini}$ and the initial bound water concentration $c_{b,ini}$, resulting from the temperature-dependent sorption isotherm (293.15 K) according to Eq. (7), were exponentially fitted [36] (see Fig. 3). The maximum values are located at the bottom and side surfaces and the lowest in the center of the TS. On contrary to $c_{v,ini}$ and $c_{b,ini}$, the initial temperature T_{ini} was assumed uniform with 293.15 K, as the temperature inside the TS was not measured (only the surrounding air temperature was logged). Moreover, it was assumed that no free water was present initially.

2.2.2. Boundary conditions

The climate surrounding the TS affects the exchange of water vapor, free water and heat at the corresponding surfaces (bottom surface and side surface, respectively). These fluxes are described with Neumann boundary conditions.

In case that a surface is exposed to free water, the infiltration flux ϕ_w is defined as:

$$\phi_w = k_{c_w}(c_w - c_{w,0})f_{lum} \tag{8}$$

with k_{c_w} as the free water mass transfer coefficient, which considers possible resistances caused by, e.g., coatings. f_{lum} is the volume proportion of the surface lumen, as free water infiltrates via the cellular tube-like lumens of wood. $c_{w,0}$ defines the concentration of free water surrounding the boundary, the maximum of which, denoted as $c_{w,max}$, is limited by a lumen entirely filled with free water:

$$c_{w,max} = f_{lum}\rho_{\mathrm{H_2O}} \tag{9}$$

As the water vapor concentration is assumed to reach its maximum quickly when free water is present at the boundary, there is no water vapor flux. Hence, defining a water vapor boundary condition is unnecessary.

Without free water at the boundary, only the water vapor flux ϕ_v has to be defined:

$$\begin{aligned} \phi_v &= k_{c_v}(c_v - c_{v,0})f_{lum} \\ \phi_w &= 0 \\ k_{c_v} &= \frac{Sh\, D_{air}\, p_{\mathrm{j}}}{L} \end{aligned} \tag{10}$$

with k_{c_v} as the mass transfer coefficient of water vapor, which takes into account air flow and convection dependent on air speed and surface roughness. $c_{v,0}$ defines the water vapor concentration of the surrounding air. Sh is the Sherwood number of 1, D_{air} describes the diffusion tensor for water vapor and L is 0.035 m (for detailed information see [21]). The parameter p_j considers the changing storage conditions occurring during the experiments (see Section 2.1), with j specifying the present climate conditions. While p_w of 0.1 describes the condition in the box in the time of wetting, $p_{d,in}$ of 0.5 and $p_{d,out}$ of 0.9 consider indoor and outdoor climate conditions, respectively, during the drying phase. Fig. 3 illustrates which parameter affects which surface depending on the climate conditions.

To account for the transition of water vapor and free water flux below and above the FSP, the smoothing function α_k is used:

$$\begin{aligned} \phi_v &= k_{c_v}(c_v - c_{v,0}) f_{lum}(1-\alpha_k) \\ \phi_w &= k_{c_v}(c_{v_{sat}} - c_{v,0}) f_{lum}\alpha_k \end{aligned} \tag{11}$$

where

$$\alpha_k = \exp(-C_{\alpha,1}(1 - c_w/1000)^{C_{\alpha,2}}) \tag{12}$$

with $C_{\alpha,1} = 20$ and $C_{\alpha,2} = 1e3$ for optimal accuracy and efficiency [21].

Energy conservation also depends on the processes previously described, which are considered with their enthalpies as follows:

$$\phi_T = k_T(T - T_0) + k_{c_v}(c_v - c_{v,0}) f_{lum}(1-\alpha_k)h_v + k_{c_v}(c_{v_{sat}} - c_{v,0}) f_{lum}\alpha_k h_v + k_{c_w}(c_w - c_{w,0}) f_{lum} h_w \tag{13}$$

with ϕ_T as the heat flux, k_T as the heat transfer coefficient of 25 $W\,m^{-2}K^{-1}$ and the temperature of the surrounding climate T_0. h_v and h_w are the enthalpies of water vapor and free water [21].

2.2.3. Glue lines

Loctite Purbond single component polyurethane (PUR) adhesive was used to glue the layers. Volkmer et al. [37] and Mannes et al. [38] showed the influence of adhesives, including PUR, on water vapor and capillary water transport, which can be significant. Therefore, glue lines are considered in the model and their effect is analyzed in Section 3.3.

2.3. Finite element model

For the simulation, only a part of the TS is modeled. Firstly, it is assumed that the fibers of the single CLT layers run in longitudinal direction of the corresponding local coordinate system, as illustrated in Fig. 3, which enables the utilization of symmetrical properties. Secondly, measurements were performed only up to a height of 150 mm. Consequently, the size of the finite element model is reduced to the left half of the TS with a height of 150 mm, originating from the bottom surface. For the drying configurations, where the bottom surface is exposed to another CLT panel, a part of a single CLT layer is additionally modeled at the bottom surface to simulate the drying conditions realistically (see Fig. 3 (c)). In this case, the output data at the end of the wetting phase were used as initial conditions for the original model part, while the initial MC of the added model part was set to 12% without free water.

Due to the reduction of the model size, the boundary conditions are only applied to the left side surface and the bottom surface. As the most significant changes in moisture and heat flux are expected at the exchange surfaces, the mesh is refined along the bottom and left side surface. In addition, the mesh at the right surface is refined for more precise values in the area of the measurement points. Therefore, the height and the width of the finite elements vary. Both are between 1 mm and 5 mm, resulting in a total number of 760 elements and 1640 nodes. In case of the expanded model, the total number of elements is increased to 1330 and the one of the nodes to 2848. The thickness of all elements is 1 mm, with only one element in the out-of-plane direction to reduce computation time. An additional simulation with a refined model, where the width and height of each element were 1 mm, showed negligible deviations between the results of the used model and the refined one.

The fiber orientation of each layer is considered, as shown in Fig. 3. It is assumed that in radial and in tangential direction the permeability of free water and diffusion are virtually equal.

2.4. Hygrothermal load

As shown in Section 2.1, the surrounding climate, the presence of free water at the bottom surface, and the contact with another CLT panel influence the moisture development of the TS. These conditions are considered by applying boundary conditions to the left and the bottom surface based on the data from the experiments (see Fig. 4 (a)). Moreover, to take into account flux resistances resulting from surrounding conditions and, thus, realistically simulate the changes in MC, the mass transfer coefficients for water vapor and free water were calibrated.

At first, the wetting phase is analyzed, with the TS exposed to free water at the bottom surface. In this case, the RH of the air only affects the left side surface, and the temperature influences both the bottom and the left surface. To simulate the water uptake through the bottom surface, the RH was set to 99% for 7 days, assuming continuous contact to water. Subsequently, the RH level was adapted according to the corresponding drying configuration (see Fig. 4 (a)). In addition, k_{c_w} as well as p_w, and thus, indirectly, the mass transfer coefficients of water vapor during the wetting phase $k_{c_{v,w}}$ were calibrated to the given climate resistances, resulting in a k_{c_w} of $1.2 \cdot 10^{-8}$ $m\,s^{-1}$ and a course of $k_{c_{v,w}}$, which can be obtained from Fig. 4 (b), with a p_w of 0.1.

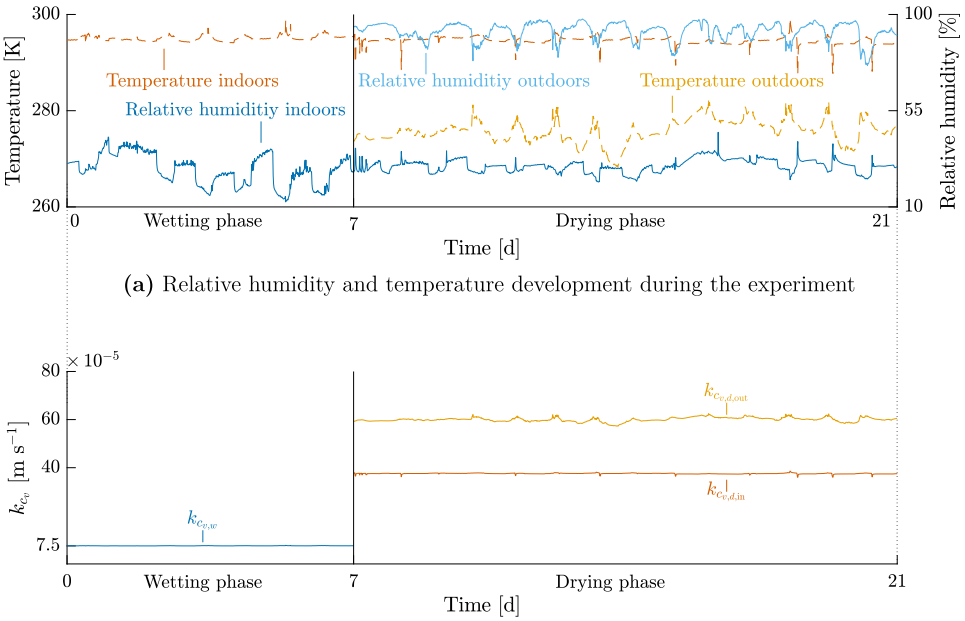

(a) Relative humidity and temperature development during the experiment

(b) Developments of the mass transfer coefficients for water vapor depending on the climate

Fig. 4. Development of the relative humidity (continuous line) and temperature (dashed line) as well as the mass transfer coefficient for water vapor k_{c_v}, which depends on relative humidity and temperature, and considers the air flow and convection of the surrounding climate. $k_{c_{v,w}}$ describes the climate in the box in the time of wetting. While $k_{c_{v,d,\text{in}}}$ considers the climate indoors during the drying phase, $k_{c_{v,d,\text{out}}}$ describes outdoor climate conditions.

Following the wetting phase, one of the four drying configurations is simulated, where the boundary conditions and coefficients are adjusted in line with the experimental setup. When all surfaces of the TS are exposed to ambient air, the corresponding indoor and outdoor climate data are applied to the left and bottom surfaces, respectively. As air speed changes due to the absence of the box and no free water could cause evaporation, the mass transfer coefficients of water vapor during the drying phase $k_{c_{v,d,in}}$ (indoor climate) and $k_{c_{v,d,\text{out}}}$ (outdoor climate) are used to consider the changing climate conditions. The development can be obtained from Fig. 4(b), with a $p_{\text{d,in}}$ of 0.5 for indoors and a $p_{\text{d,out}}$ of 0.9 for outdoor climate conditions. Both parameters were calibrated to their corresponding climate conditions. When the TS are in contact with another CLT panel, the following adjustments were made to consider these conditions realistically: Rather than applying a boundary condition, a part of a single CLT layer is additionally modeled at the bottom surface (see Fig. 3). For the left side surface, the corresponding indoor and outdoor climate data, as well as their respective transfer coefficients, are used.

To study the influence of adhesives between layers, additional simulations were performed, where for the elements representing glue lines the free water flow properties and water vapor diffusion values of Lukacevic et al. [39] were used. For free water flow in longitudinal direction, $\boldsymbol{J}_{\boldsymbol{w}_L}$ was reduced by a factor of $3 \cdot 10^{-4}$, as described in Lukacevic et al. [39].

3. Results and discussion

In order to compare and analyze the results of the finite element simulations and the experiments, MC distributions have to be determined, as the simulation output is bound water concentration (c_b), water vapor concentration (c_v) and free water concentration (c_w). MC is the sum of bound water concentration and free water concentration divided by the dry density of wood (ρ_d): $MC = (c_b + c_w)/\rho_d$.

3.1. Comparison of experimental and simulation results

The MC simulation results of all four drying configurations are shown in Figs. 5–8, obtained from finite element nodes at a height of 30 mm, 60 mm and 90 mm, respectively, at a depth of 5 mm from the surface (S) and at a depth of 50 mm from the surface in the middle layer (M). The moisture behavior at 120 mm as well as 150 mm are not illustrated, since the MC evolution between these and at 90 mm differs only minimally. For all drying configurations, the MC changes of the three TS used for the corresponding scenario (gray lines), the average of these three TS (teal line) and the average of all twelve TS during the wetting phase, lasting from the beginning until day 7 (orange line), are displayed. The squares along the lines represent the measured values from the experiment, and the blue line displays the simulation MC development. In addition, during the calibration process, efforts were made to attain MC values close to, ideally slightly exceeding the average experimental results to consider a unfavorable moisture uptake behavior of the TS, as strength and stiffness properties are impaired. Furthermore, for each simulation, the mean absolute error (MAE) and

the root mean square error (RMSE) are provided to quantify the performance of the simulation results. They are determined as follows:

$$\mathrm{MAE} = \frac{1}{n}\sum_{t=1}^{n}\left|f_t - y_t\right|$$
$$\mathrm{RMSE} = \sqrt{\frac{1}{n}\sum_{t=1}^{n}\left(f_t - y_t\right)^2} \tag{14}$$

Here, n represents the number of measurements. f_t denotes the simulated data, and y_t defines the measured data for the points in time of measurement t. y_t consists of the average experimental result of all twelve TS (from days 0 to 7) as well as the average of the three TS subjected to the corresponding climate configuration (from days 7 to 21). MAE and RMSE are suitable indicators since the data were measured at sufficiently equal intervals and there are no scale differences.

At first, the drying configuration with the bottom surface exposed to indoor air is analyzed (see Fig. 5). Due to equal boundary conditions for all experimental configurations during the wetting phase, its results are only described for this configuration (except for the configuration with the bottom surface exposed to outdoor climate conditions due to extensive moisture uptake of one of the TS; see Fig. 6 (a)). Analyzing the initial MC behavior in Fig. 5 (a) at a depth of 5 mm from the surface and a height of 30 mm (S_{30}) shows that, in the very beginning, both the simulation and the average experimental results decrease. This is related to the surrounding dry climate and the non-immediate moisture penetration into this area. However, while the average MC of all experiments increases after 8.25 h, the one of the simulation decreases until 1.50 days. An extensive moisture uptake, observed for the extreme case of the individual experiments, can be simulated by adapting k_{c_w}, which is further examined in Section 3.2. After 5.5 days, the MC increase rate decreases significantly, as from this point on, the bound water concentration has reached its limit, and only the free water concentration increases. After seven days, the storage conditions change, resulting in a reduction in MC. In Fig. 5 (b), it can be seen that the average experimental and the simulated MC initially decrease at S_{60}. While the average MC of the experiments increases after 1.25 days and decreases again after 2.25 days, the simulation MC increases only after 4.25 days and falls when the drying phase starts. The increase and decrease during the wetting phase of the average experimental MC is caused by averaging all MC developments of the investigated TS, since the moisture absorption of some CLT panels is disproportionately intense in the first days due to their boards' wood anatomy (fiber size and orientation, knots, etc.) Fig. 5 (c) also displays an initial reduction of the MC at S_{90}. However, compared to Fig. 5 (a) and (b), no significant increase during the wetting phase can be seen, indicating that capillary forces are not sufficient to lift free water to this level in a timely manner. Fig. 5 (d) illustrates that the initial MC at M_{30} increases immediately when the TS are immersed in water since the layer at 50 mm depth is only affected by the

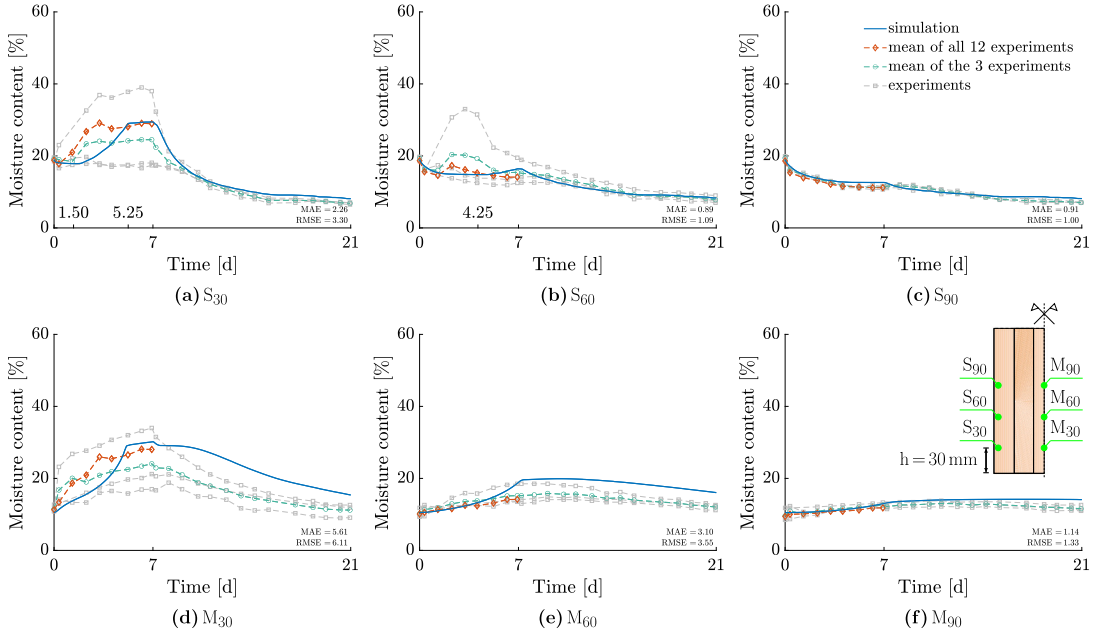

Fig. 5. Results for Group A (see Table 1) - Simulated and measured moisture content during the wetting phase (0–7 days) and the drying phase (7–21 days) in indoor climate conditions with the bottom surface exposed to air. The gray lines show the moisture development of the three test specimens subjected to these conditions, the teal line displays their average, and the orange curve illustrates the average moisture evolution of all experiments (12 in total) during the identically proceeding wetting phase. (f) shows the positions of the nodes from which the simulation results were obtained (S_i: surface measurement points at a height of i mm, M_i: measurement points located in the middle layer at a height of i mm). (For interpretation of the references to color in this figure legend, the reader is referred to the web version of this article.)

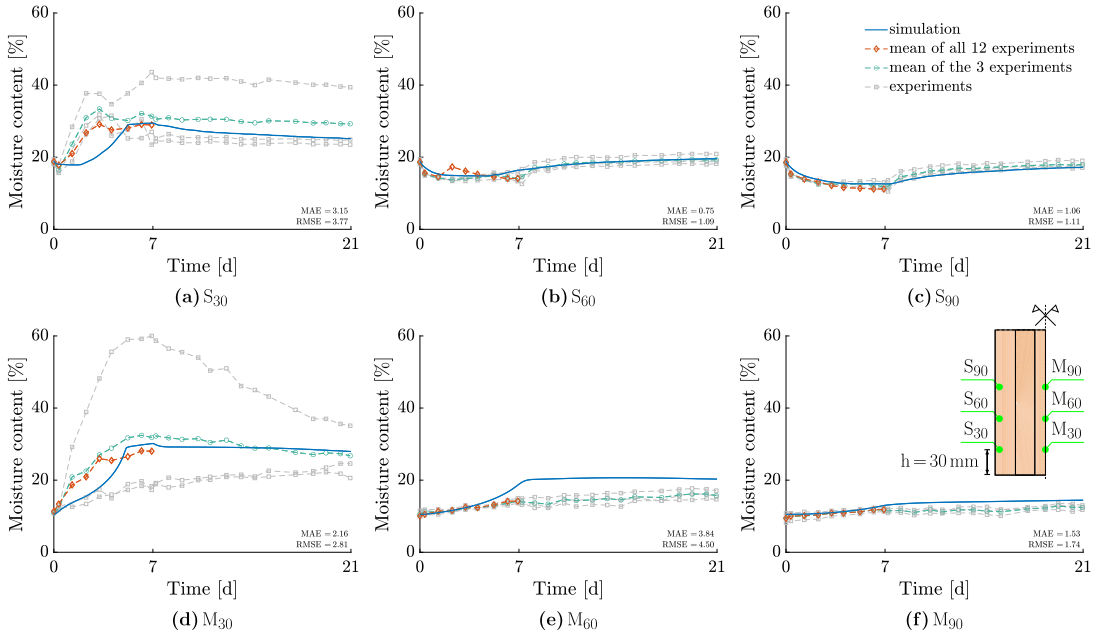

Fig. 6. Results for Group B (see Table 1) - Simulated and measured moisture content during the wetting phase (0–7 days) and the drying phase (7–21 days) in outdoor climate conditions with the bottom surface exposed to air. The gray lines show the moisture development of the three test specimens subjected to these conditions, the teal line displays their average, and the orange curve illustrates the average moisture evolution of all experiments (12 in total) during the identically proceeding wetting phase. (f) shows the positions of the nodes from which the simulation results were obtained (S_i: surface measurement points at a height of i mm, M_i: measurement points located in the middle layer at a height of i mm). (For interpretation of the references to color in this figure legend, the reader is referred to the web version of this article.)

low RH of the surrounding climate after a certain amount of time, which is longer than the wetting phase. However, compared to the moisture uptake of the experimental results, the one of the simulation occurs slower, as it was aimed to obtain MC values close to, ideally slightly above, the average experimental results at the end of the wetting phase to consider an unfavorable infiltration behavior of the TS. Increasing k_{c_w} causes a more similar moisture uptake rate of the average experimental and simulations results during the wetting phase, which is shown in Section 3.2. In the drying phase, the decrease rate of the experimental average MC and the simulation one are alike, except for the first two days of this phase. During this time, a significant decrease in the simulation MC occurs, followed by an intense flattening of the development. During the significant decline, the entire free water disappears, and after that, only the bound water decreases, which is initially minimally reduced due to slower desorption close to the FSP [29,40] and because of the insignificant influence of the air with low RH.

Overall, the simulation results qualitatively align well with the average outcome of the experiments for this drying configuration.

Fig. 6 displays the results of the drying configuration, where the bottom surface is exposed to outdoor climate conditions. Analyzing the drying phase of Fig. 6 (a) shows that the moisture decreases only minimally compared to Fig. 5 (a) due to the outdoor climate's higher RH level. In addition, it can be noticed that the simulation MC is lower than the average experimental one throughout the drying phase. This is related to the relatively extensive MC uptake of the three TS in the wetting phase compared to the other drying configurations (see Figs. 5 (a), 7 (a) and 8 (a)). Fig. 6 (b) and (c) reveal an increasing MC during the drying phase due to the outdoor climate's high RH, and the simulation results are only minimally lower compared to the average experimental results.

Except for the discussed MC behavior in Fig. 6 (a) caused by the intense moisture uptake of one experiment, a great qualitative agreement of the simulation and average experimental results can be seen. It might be possible that the great variability of the measurement results are due to the natural irregularity of the wood material properties, which further emphasizes the need for the sensitivity analysis presented in Section 3.2, or due to the limitations of the electrical resistance-based MC measurement.

Fig. 7 displays the moisture development results when the bottom surface is exposed to a CLT panel and the remaining surfaces are subjected to indoor climate conditions. Adding an additional part of a CLT layer to the finite element model at the bottom surface causes a lower MC reduction in the drying phase, where with increasing distance to the bottom surface, the effect decreases. While the difference in MC at M_{30} is about 6.5% at the end of the drying phase (compare Figs. 5 (d) and 7 (d)), the difference in MC is only 0.1% at M_{90} (compare Figs. 5 (f) and 7 (f)). In addition, the effect of the additional model part is more significant for the middle layer than for the surface layer. The maximum difference at S_{30} is only about 1.8% at the end of the drying phase (see Fig. 5 (a)).

Similarly for this configuration, simulation results exhibit a good qualitative correlation with the average findings of the experiments.

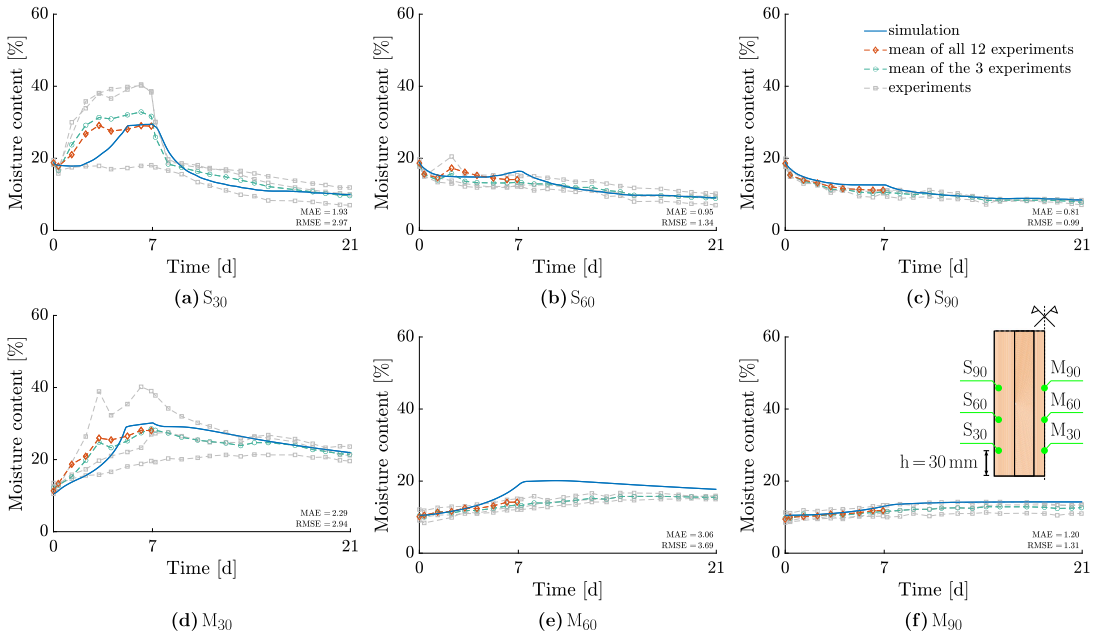

Fig. 7. Results for Group C (see Table 1) - Simulated and measured moisture content during the wetting phase (0–7 days) and the drying phase (7–21 days) in indoor climate conditions with the bottom surface exposed to a CLT panel. The gray lines show the moisture development of the three test specimens subjected to these conditions, the teal line displays their average, and the orange curve illustrates the average moisture evolution of all experiments (12 in total) during the identically proceeding wetting phase. (f), shows the positions of the nodes from which the simulation results were obtained (S_i: surface measurement points at a height of i mm, M_i: measurement points located in the middle layer at a height of i mm). (For interpretation of the references to color in this figure legend, the reader is referred to the web version of this article.)

Finally, in Fig. 8, the MC results are shown when the bottom surface is fixed to a CLT panel and the remaining surfaces are subjected to outdoor climate conditions. Compared to the configuration, where the CLT panel is exposed to indoor climate conditions, the effect of the additional model part is smaller (see Fig. 7). At the end of the drying phase, the difference in MC of both outdoor configuration simulation results is only between 0.59% and 0.06%, while the one of the indoor configurations is between 6.52% and 0.1%. Fig. 8 (a) shows that after 10.75 days the simulation MC is lower than the average experimental one due to the moisture uptake of two TS in the drying phase influencing the average.

Apart from the MC behavior at S_{60} and S_{90} (see Fig. 8 (b) and (c)) due to too low moisture uptake, a good qualitative agreement of the simulation results with the average experimental ones can be noticed.

The results show elevated MC levels surpassing the FSP at 30 mm from the bottom surface, for particular experimental cases even at a height of 60 mm. Sandberg and Saline [41] observed similar MC behavior in their experiments, examining the MC absorption through the end-grain surface of Norway spruce boards. After seven days of wetting, the MC profiles reveal MC levels above the FSP up to 50 mm from the infiltration surface. Krabbenhoft and Damklide [32] introduced a double-porosity model to describe water infiltration and used different experiments to validate their model. The presented moisture profile of fir sapwood revealed an MC level greater than 30% at a height of 125 mm from the infiltration surface after six days. Johansson and Kifetew [42] modeled the capillary water uptake in wood based on CT scans, showing MC levels exceeding the FSP at 90 mm from the bottom surface for pine sapwood. It can be concluded that (CLT) end-grain wetting establishes a decay-prone area close to the infiltration surface, thus, illustrating the relevance of moisture safety in this zone.

Additionally, an evaluation of the performance of MAE and RMSE for all configurations (see Figs. 5–8) shows an adequate correlation for S_{60} (MAE ranging from 0.75 to 1.33 and RMSE from 1.09 to 1.48) and S_{90} (MAE from 0.81 to 1.80 and RMSE from 0.99 to 1.92). There is also a sufficient replication quality for M_{90} (MAE from 1.14 to 1.92 and RMSE from 1.31 to 2.22). However, high MAE and RMSE values can be observed at S_{30}, M_{30} and M_{60}, with values up to 5.61 and 6.11, respectively. These discrepancies can be attributed to the focus of the calibration process. For the wetting phase, efforts targeted achieving MC values close to – or ideally slightly above – the average experimental results of all twelve TS. Meanwhile, for the drying phase, the parameters were calibrated to mirror the average experimental results of the three TS corresponding to the specific climate conditions. As a result, significant differences between y_t and f_t can arise, affecting MAE and RMSE. Additionally, variations in wood properties can lead to a high degree of variability in experimental results, impacting the determined averages. With a limited number of investigated TS, MAE and RMSE might suggest a reduced correlation.

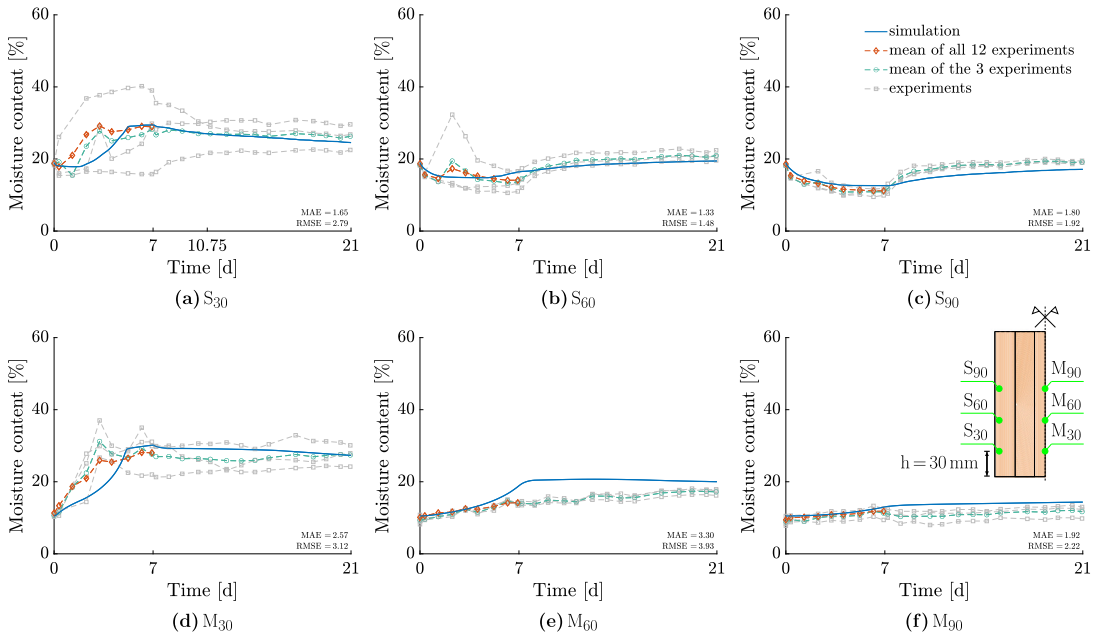

Fig. 8. Results for Group D (see Table 1) - Simulated and measured moisture content during the wetting phase (0–7 days) and the drying phase (7–21 days) in outdoor climate conditions with the bottom surface exposed to a CLT panel. The gray lines show the moisture development of the three test specimens subjected to these conditions, the teal line displays their average, and the orange curve illustrates the average moisture evolution of all experiments (12 in total) during the identically proceeding wetting phase. (f) shows the positions of the nodes from which the simulation results were obtained (S_i: surface measurement points at a height of i mm, M_i: measurement points located in the middle layer at a height of i mm). (For interpretation of the references to color in this figure legend, the reader is referred to the web version of this article.)

3.2. Sensitivity analysis

Subsequently, the impact of the mass transfer coefficients of water vapor k_{c_v} and free water k_{c_w} on the moisture development is shown. To depict the degree of this influence, both coefficients are doubled and halved, respectively. Fig. 9 shows the impact of increasing and reducing k_{c_w} and k_{c_v}, respectively, on the MC development when the bottom surface is exposed to air and indoor climate conditions. In each case, the green curves show the MC evolution if the value is increased, while the magenta lines display the MC change for a reduced value. The blue curves depict the MC development with the original choice of coefficients, presented in Section 2.4, and the orange, teal and gray lines illustrate the same as described in Section 3.1. First, the influence of increasing and decreasing k_{c_w} at S_{30} is discussed (see Fig. 9 (a)). k_{c_w} considers infiltration resistances due to, e.g., coatings. Adapting k_{c_w} enables to obtain moisture uptakes comparable to the MC evolution of single experiments corresponding to the extreme cases. Fig. 9 (a) illustrates the MC development in case of increasing k_{c_w} from $1.2 \cdot 10^{-8}\,\mathrm{m\,s^{-1}}$ to $2.4 \cdot 10^{-8}\,\mathrm{m\,s^{-1}}$ at S_{30}. It can be seen that the simulation MC also decreases initially, but the following intense moisture uptake occurs already approximately 0.75 days later. After about two days, the FSP is reached, and from this point on, only the concentration of free water increases, which is why the MC increases more slowly. Further increasing k_{c_w} to $3.6 \cdot 10^{-8}\,\mathrm{m\,s^{-1}}$ would result in an MC development comparable to the experiment with intense moisture uptake. By reducing k_{c_w} to $6 \cdot 10^{-9}\,\mathrm{m\,s^{-1}}$, the MC development of two experiments with low moisture uptake can be simulated. Fig. 9 (b) displays the MC evolution with adapted k_{c_w} at M_{30}. At the end of the wetting phase, the MC is slightly above the experiment results, showing that even the experiment with the more significant moisture uptake could be simulated. Observing the MC development with reduced k_{c_w}, a minimal increase of the MC after the beginning of the drying phase can be seen. Since the low RH affects the MC in M_{30} only after a specific time, the MC does not drop until about 9.75 days. Kalbe et al. [19] showed an MC plateau (approximately 25%) at M_{30} three days after the beginning of the wetting phase. The sensitivity analysis reveals that this is related to the FSP on the one hand and, on the other hand, to the intensity of the free water increase driven by capillary pressure [21].

However, for S_{60} (see Fig. 9 (c)) and for the other studied locations (S_{90}, M_{60}, and M_{90}), a moisture uptake of up to about 32% in the wetting phase occurs as well since k_{c_w} determines the intensity of the free water flux at the bottom surface. It is possible to obtain simulation results comparable to extreme cases of single experimental results at a height of 30 mm, if k_{c_w} is increased correspondingly. However, this also leads to excessive MC values above 30 mm from the bottom surface. If the bottom surface is immersed in water, extensive infiltration in regions close to the water source can be noticed [32,41,43] (see Fig. 1 (c)). As described in [21], the model used is not able to adequately consider intense moisture uptake in these regions correspondingly. For this reason, the average experimental and simulation results agree at S_{30} only after about 5 days during the wetting phase. Sandberg and Saline [41] studied moisture absorption in the end-grain of Norway spruce, using CT scanning for measurement. Their measured

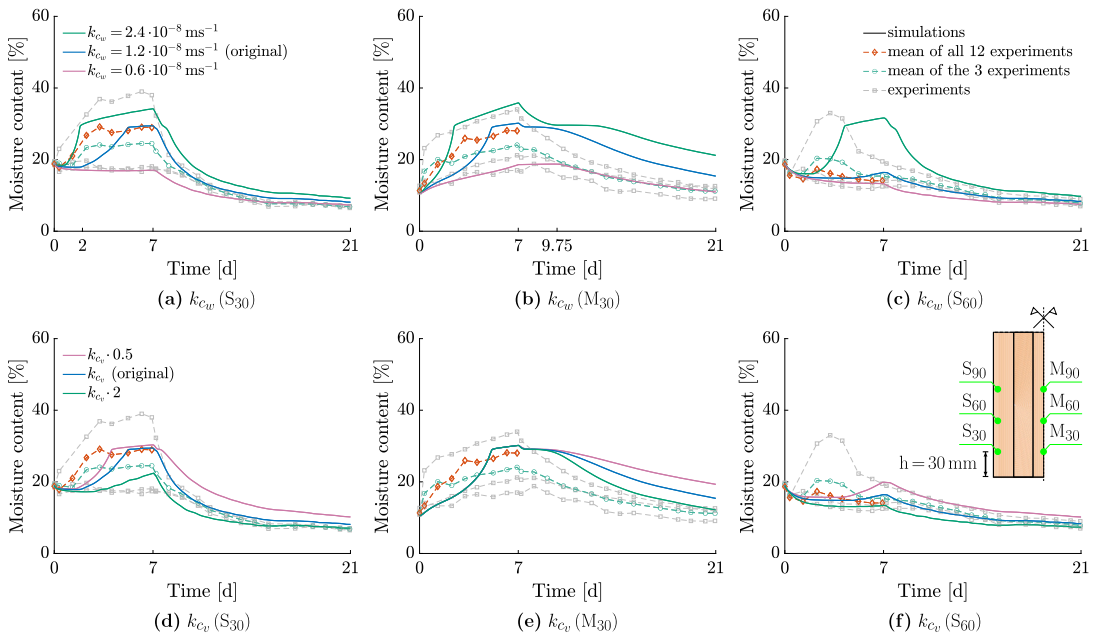

Fig. 9. Sensitivity analysis — Moisture content at various heights and depths when different parameters ((a) to (c): mass transfer coefficient for free water k_{c_w}, and (d) to (f) mass transfer coefficient for water vapor k_{c_v}) are altered for bottom surface exposure to air and indoor climate conditions. Continuous lines illustrate simulation results and dashed lines with markers experimental results. In addition, the MC changes of the three test specimens (TS) used for the corresponding scenario (gray lines), the average of these three TS (teal line) and the average of all TS during the wetting phase, lasting from the beginning until day 7 (orange line), are displayed. (f) shows the positions of the nodes from which the simulation results were obtained (S$_i$: surface measurement points at a height of i mm, M$_i$: measurement points located in the middle layer at a height of i mm). (For interpretation of the references to color in this figure legend, the reader is referred to the web version of this article.)

MC profiles and our simulation results agree well at 40 mm from the water level. Perre et al. [43] examined the imbibition of water and oil in poplar and spruce wood TS in longitudinal direction and used a Washburn simulation approach to replicate the water uptake. Comparing the simulation results under corresponding conditions shows that the moisture uptake replicated by our model is underestimated close to the infiltration surface.

Subsequently, the impact of adapting k_{c_v} on the MC development is discussed. It is evident that doubling k_{c_v} causes a lower moisture uptake in the wetting phase and a slower dry-out in the drying phase, while halving k_{c_v} results in the opposite effect (Fig. 9 (d) and (f)). This is caused by the low relative humidity: Doubling k_{c_v} increases the water vapor flux at the exchange surface, which leads to a decrease in the water vapor concentration due to the environmental adjustment and, thus, to a lower concentration of bound water. In case of higher RH values, an increased k_{c_v} would cause a more extensive moisture uptake in the wetting phase and less dry-out during the drying phase. Fig. 9 (e) illustrates the influence of adapting k_{c_v} at M$_{30}$. As the surrounding air only affects the moisture uptake in the middle layer after an extensive amount of time (longer than the wetting phase), no difference can be observed during the wetting phase. Only in the drying phase, when the bottom surface is exposed to air, increasing k_{c_v} results in a more significant dry-out, while decreasing k_{c_v} causes minor MC reductions.

It can be concluded that both coefficients influence the MC development, but k_{c_w} is primarily related to an intense MC uptake, which is essential to reproduce the experimentally observed MC behavior realistically.

Another value to quantify the intensity of moisture uptake, is the water absorption coefficient A$_w$. It is defined as the difference in moisture mass over time divided by the infiltration surface and related to the square root of time according to EN ISO 15148 [22]. According to the study of Candanedo and Derome [44], where the moisture uptake of 14 softwood samples were examined, A$_w$ ranges between $9.7 \cdot 10^{-3}$ kg m^{-2} s$^{-0.5}$ and $1.6 \cdot 10^{-2}$ kg m^{-2} s$^{-0.5}$ in longitudinal direction, whereas in radial and tangential direction, A$_w$ is between $1.9 \cdot 10^{-3}$ kg m^{-2} s$^{-0.5}$ and $4.7 \cdot 10^{-3}$ kg m^{-2} s$^{-0.5}$. In contrast to sawn timber, the water absorption coefficient for CLT panels, exposing the face-grain surface to water, diverges. For CLT samples made of European wood, A$_w$-measurements range from $1.6 \cdot 10^{-3}$ kg m^{-2} s$^{-0.5}$ to $1.1 \cdot 10^{-8}$ kg m^{-2} s$^{-0.5}$ [45–47]. For water absorption through the end-grain surface of CLT panels, the only water absorption coefficient available to date is the one determined from the experiments presented in this work (see Section 2.1), which is $3.51 \cdot 10^{-3}$ kg m^{-2} s$^{-0.5}$ [25]. Calculating A$_w$ based on the simulation results, a lower value can be observed ($1.23 \cdot 10^{-3}$ kg m^{-2} s$^{-0.5}$). This is related to the not yet implemented intense moisture uptake in the regions close to infiltration surfaces. Thus, enhancing the model to describe the free water transport processes in the infiltration area more precisely, would result in a higher and more accurate water absorption coefficient.

One of the limitations of this study, which also impedes the validation of the implementation of the intense moisture uptake near the infiltration surfaces, is the use of electrical resistance-based measurements for obtaining wood MC. Change in electrical

resistance caused by a variation in wood MC is greatest up to 30% MC, diminishing as the MC increases, which reduces measurement accuracy [48]. However, MC exceeds this level quickly near the infiltration surface. Other constraints of the method include the variability in the relationship between electrical resistance and wood MC due to the specific timber species, temperature, density, or variations in calibration. Gravimetric MC measurement method would have been the most accurate in terms of MC. However, it would have required cutting the TS into smaller details to obtain MC distribution information, which would have only been achievable at the end of the test, rendering the analysis of MC temporal kinetics impossible. Furthermore, additional uncertainty would have also been introduced by cutting off the TS. On the contrary, the electrical resistance-based method enabled MC measurements at precise height and depth levels with minimal damage and effort. This also facilitates the method's application on construction sites and the use of the collected data as an input for hygrothermal models, which may then be used, for instance, to forecast moisture dry-out and wetting incidents, which is one of the main purposes of the model described in this article. In addition, research has shown that resistance-based MC measurements can still be useful in the overhygroscopic range [49]. Considering the limitations and advantages, the electrical resistance-based method was deemed suitable. Nevertheless, novel non-destructive MC measurement methods could help to improve this work, specifically regarding MC distribution near the CLT face-grain surface, where the MC quickly reaches the FSP in case of water contact. Such methods include low field nuclear magnetic resonance (LFNMR), X-ray computed tomography (XCT), neutron imaging, and magnetic resonance imaging (MRI) [48]. Implementing LFNMR to determine MC could further improve the model, as LFNMR can differentiate between different water states [50], enabling fine-tuning of k_{c_v} and k_{c_w}, respectively, especially close to the infiltration surfaces. However, these methods come with their own set of limitations regarding calibration or specimen size, which need consideration. In addition, the experimental setup might need thorough rework if new MC measurement methods would be used.

3.3. Influence of glue on moisture transport

In addition to the effect of k_{c_v} and k_{c_w}, the influence of the glue lines on the moisture transport is analyzed, which is shown in Fig. 10. The studied configuration is characterized by indoor climate conditions and the bottom surface is subjected to the surrounding air. The blue line shows the MC development with the parameter set used in Section 3.1, while the turquoise curve illustrates the effect of the reduced glue line permeability and vapor diffusion. The orange, teal and gray lines represent the experimental results as presented in Section 3.1. Compared to the original value set, the glue line consideration has only a minor influence on the MC development at S_{30}, S_{60}, and S_{90} (see Fig. 10 (a) to (c)), as the proximity of the air with low relative humidity and the water infiltration mainly contribute to the moisture behavior at the surface. In the middle layer, the glue line affects the MC development more significantly due to the minor effect of the surrounding dry air. Overall, the trend of the MC curves with

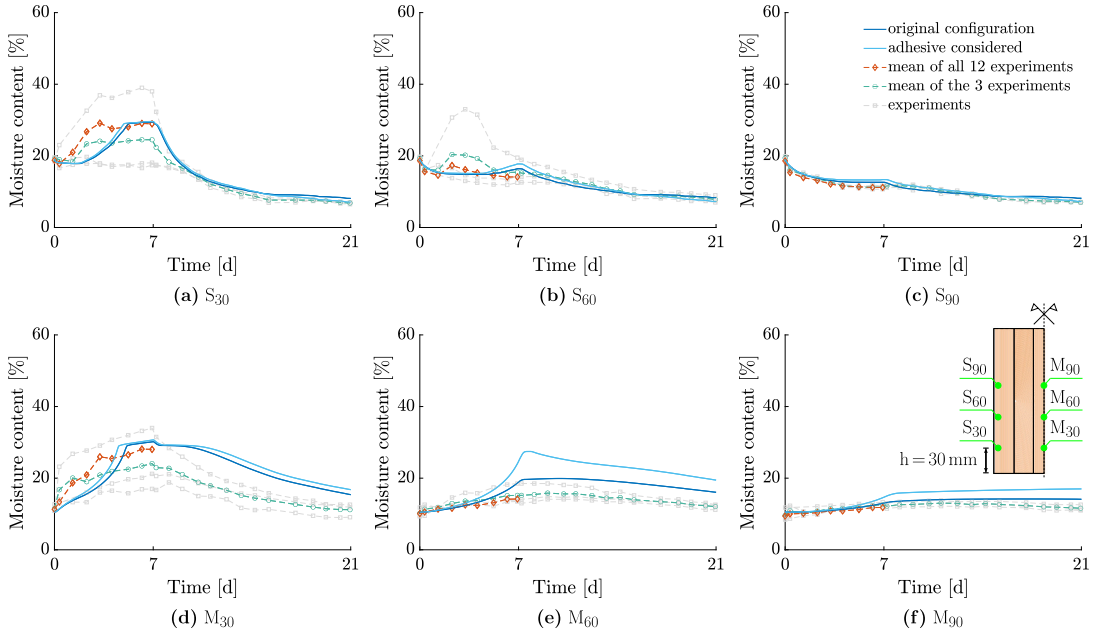

Fig. 10. Glue influence — Simulation and experiment moisture contents during the wetting phase (0–7 days) and the drying phase (7–21 days; indoor climate conditions with the end-grain surface exposed to air). While the blue line shows the MC development with the setup used in Fig. 5, the turquoise curve illustrates the MC change if additionally the reduced permeability of the glue is considered. Dashed lines with markers illustrate experimental results (see Fig. 5). (f) shows the positions of the nodes from which the simulation results were obtained (S_i: surface measurement points at a height of i mm, M_i: measurement points located in the middle layer at a height of i mm). (For interpretation of the references to color in this figure legend, the reader is referred to the web version of this article.)

the initial configuration and the one considering the reduced permeability and diffusion of the glue line is quite similar, and the influence is minor at the surface and moderate in the middle layer. As the exact parameter values for permeability and vapor diffusion are unknown, the influence on MC development may be larger or smaller. However, as more conservative values were used, it is assumed that the evolution is correct or closer to the one without the consideration of glue lines. Additional simulations confirmed that similar MC trends can be observed for the other drying configurations.

4. Conclusion & outlook

High moisture contents (MC) can compromise cross-laminated timber (CLT) elements, and end-grain wetting can pose particular challenges due to moisture trapping conditions often present in the connection joints where the CLT end-grain surfaces are located (e.g., in wall-to-foundation or wall-to-floor joints). Research is scarce regarding the moisture safety of CLT end-grain surfaces. To investigate end-grain wetting conditions, in this work, the numerical model considering free water transport of Autengruber et al. [21] was adapted for a more sophisticated problem–replicating the CLT end-grain moisture uptake and dry-out experiments of Kalbe et al. [19]. The experiments included the investigation of MC development in CLT panels and panel junctions with moisture trapping conditions, considering both favorable and unfavorable climate conditions regarding moisture dry-out. The utilized numerical model is based on the multi-Fickian theory [26–31] for bound water and water vapor diffusion processes below the fiber saturation point (FSP) as well as on Darcy's law combined with a concentration-based formulation for free water transport above the FSP. The calibration of the mass transfer coefficients of water vapor k_{c_v} and free water k_{c_w} allowed for the simulation of MC changes in CLT test specimens during an initial wetting phase (from days 0 to 7), followed by a drying phase (from days 7 to 21), which was characterized by different climate and storage conditions. Furthermore, the influence of k_{c_v} and k_{c_w} on the MC behavior was examined, and finally, the effect of glue lines on the MC transport was studied by reducing values for permeability and vapor diffusion.

The main conclusions can be summarized as follows:

- The simulation results demonstrate strong qualitative agreement with the experimental outcomes for moisture uptake and dry-out across all investigated configurations. In certain cases, even excellent replication was observed. Hence, such simulations can be used to gain deeper understanding of moisture distributions in CLT panels, thus supporting safety and durability issues of CLT structures.
- The results support the relevance of moisture safety regarding the CLT end-grain surfaces, showing MC levels reaching or exceeding the FSP at 30 mm from the water level, thus rendering this region susceptible to decay. However, the risk is localized, as capillary forces appear insufficient to lift free water to the 90 mm mark from the water level, as suggested by the results.
- The MC plateau ($\approx$ 25%) at 30 mm from the water level in the middle CLT layer observed in the experimental results of Kalbe et al. [19] could be related to both the FSP and the intensity of the free water increase driven by capillary pressure.
- The coefficients k_{c_v} and k_{c_w} exert a notable influence on the MC evolution. However, it is mainly k_{c_w}, the mass transfer coefficient of free water, that significantly contributes to the intense moisture uptake. This factor is critical for realistically reproducing the MC behavior above the FSP.
- The impact of glue lines on the moisture behavior of CLT surface layers is marginal but becomes more pronounced in the middle layers. Despite this, the effect of glue lines is smaller than the one of the investigated mass transfer coefficients (k_{c_v} and k_{c_w}).

Additional experiments are recommended to validate the model results, particularly data from measurement points located at positions with fiber orientations different than those investigated during the experiments of Kalbe et al. [19]. To provide a more comprehensive data set, measurement points closer to the end-grain surface and with increased spatial resolution are suggested.

Continued work is needed to ensure an appropriate moisture management method for the CLT end-grain surfaces. Future simulations and experiments should assess the influence of extended and abbreviated wetting and drying phases. In addition, further investigation is recommended regarding different boundary condition configurations in conjunction with long-term simulations. Furthermore, additional boundary conditions could be considered, e.g., precipitation and solar radiation or the influence of sealing of the CLT panel end-grain surfaces. Water-blocking coatings have been suggested as a moisture safety method to protect the CLT panel end-grain surfaces [51], and a natural progression of this work would be to assess the performance of such protection methods. More broadly, research is needed to compare the performance of local protection methods with full coverage weather protection (e.g., using a tent or scaffolding to cover the CLT after installation).

Beyond moisture simulations, fracture simulations could be performed, to investigate the cracking behavior in the drying phase, as presented in Brandstätter et al. [52]. In this work, the moisture-induced cracking behavior of wooden cross sections exposed to various drying loads was analyzed, using a multisurface failure criterion [53–56], which was also applied in the studies of Autengruber et al. [57], to define failure. This way, the optimal point in time could be determined to apply heating and, thus, speed up the dry-out of CLT panels without causing cracks [19].

CRediT authorship contribution statement

Florian Brandstätter: Writing – original draft, Writing – review & editing, Visualization, Software, Investigation, Methodology. **Kristo Kalbe:** Writing – original draft, Writing – review & editing, Visualization, Methodology, Investigation, Conceptualization. **Maximilian Autengruber:** Supervision, Conceptualization, Methodology, Writing – review & editing, Software. **Markus Lukacevic:** Supervision, Conceptualization, Methodology, Writing – review & editing. **Targo Kalamees:** Writing – review & editing, Methodology, Supervision, Project administration, Funding acquisition. **Aime Ruus:** Investigation. **Alvar Annuk:** Investigation. **Josef Füssl:** Supervision, Conceptualization, Methodology, Writing – review & editing, Funding acquisition, Project administration.

Declaration of competing interest

None of the authors have any potential conflicts of interest or competing interests.

Data availability

Data will be made available on request.

Acknowledgments

The fundings from the Austrian Science Fund (FWF) through the START project Y1093-N30, Austria are gratefully acknowledged. The experimental part of this work received funding from the Estonian Centre of Excellence in Zero Energy and Resource Efficient Smart Buildings and Districts, ZEBE, Estonia (grant No. 2014–2020.4.01.15-0016) and by the Estonian Research Council, Estonia (grant No. PRG483, Moisture safety of interior insulation, constructional moisture and thermally efficient building envelope). Arcwood by Peetri Puit OÜ is acknowledged for the delivery of the CLT panels for the laboratory study.

References

[1] F. Asdrubali, B. Ferracuti, L. Lombardi, C. Guattari, L. Evangelisti, G. Grazieschi, A review of structural, thermo-physical, acoustical, and environmental properties of wooden materials for building applications, Build. Environ. 114 (2017) 307–332, http://dx.doi.org/10.1016/j.buildenv.2016.12.033, URL https://www.sciencedirect.com/science/article/pii/S0360132316305285.

[2] T. Scheffer, J. Morrell, Natural Durability of Wood:a worldwide Checklist of species, Tech. rep., Forest Research Laboratory, Oregon State University. Research Contribution 22, 1998, URL https://ir.library.oregonstate.edu/concern/technical_reports/dz010r37p.

[3] H. Guo, Y. Liu, Y. Meng, H. Huang, C. Sun, Y. Shao, A comparison of the energy saving and carbon reduction performance between reinforced concrete and cross-laminated timber structures in residential buildings in the Severe Cold Region of China, Sustainability 9 (8) (2017) http://dx.doi.org/10.3390/su9081426, URL https://www.mdpi.com/2071-1050/9/8/1426.

[4] M.F.L. Mallo, O. Espinoza, Cross-laminated timber vs. concrete/steel: Cost comparison using a case study, in: Proceedings of the World Conference on Timber Engineering, WCTE, Vienna, Austria, 2016, pp. 22–25.

[5] H.R. Lu, A. El Hanandeh, B.P. Gilbert, A comparative life cycle study of alternative materials for Australian multi-storey apartment building frame constructions: Environmental and economic perspective, J. Clean. Prod. 166 (2017) 458–473, http://dx.doi.org/10.1016/j.jclepro.2017.08.065, URL https://www.sciencedirect.com/science/article/pii/S095965261731781X.

[6] S. Reichel, Modellierung und Simulation hygro-mechanisch beanspruchter Strukturen aus Holz im Kurz- und Langzeitbereich (Ph.D. thesis), Technische Universität Dresden, 2015.

[7] C. Gerhards, Effect of moisture content and temperature on the mechanical properties of wood: an analysis of immediate effects, Wood Fiber 14 (1) (1982) 4–36.

[8] M. Autengruber, M. Lukacevic, C. Gröstlinger, J. Füssl, Finite-element-based prediction of moisture-induced crack patterns for cross sections of solid wood and glued laminated timber exposed to a realistic climate condition, Constr. Build. Mater. 271 (2021) 121775, http://dx.doi.org/10.1016/j.conbuildmat.2020.121775, URL https://www.sciencedirect.com/science/article/pii/S095006182033779X.

[9] M. Fragiacomo, S. Fortino, D. Tononi, I. Usardi, T. Toratti, Moisture-induced stresses perpendicular to grain in cross-sections of timber members exposed to different climates, Eng. Struct. 33 (11) (2011) 3071–3078, http://dx.doi.org/10.1016/j.engstruct.2011.06.018, Modelling the Performance of Timber Structures. URL https://www.sciencedirect.com/science/article/pii/S0141029611002549.

[10] H. Blaß, C. Sandhaas, Ingenieurholzbau - Grundlagen der Bemessung, KIT Scientific Publishing, 2016.

[11] K. Gradeci, N. Labonnote, B. Time, J. Köhler, Mould growth criteria and design avoidance approaches in wood-based materials – A systematic review, Constr. Build. Mater. 150 (2017) 77–88, http://dx.doi.org/10.1016/j.conbuildmat.2017.05.204, URL https://www.sciencedirect.com/science/article/pii/S0950061817311029.

[12] M.S. Austigard, J. Mattsson, Fungal damages in Norwegian massive timber elements – a case study, Wood Mater. Sci. Eng. 15 (6) (2020) 326–334, http://dx.doi.org/10.1080/17480272.2020.1801835.

[13] J.E. Gaarder, T.D. Pettersen, Built-in moisture in cross-laminated timber roofs – a field study, 2069, 2021, p. 8, http://dx.doi.org/10.1088/1742-6596/2069/1/012051, 012051,

[14] L. Wang, H. Ge, Hygrothermal performance of cross-laminated timber wall assemblies: A stochastic approach, Build. Environ. 97 (2016) 11–25, http://dx.doi.org/10.1016/j.buildenv.2015.11.034, URL https://www.sciencedirect.com/science/article/pii/S0360132315301967.

[15] L. Wang, H. Ge, Stochastic modelling of hygrothermal performance of highly insulated wood framed walls, Build. Environ. 146 (2018) 12–28, http://dx.doi.org/10.1016/j.buildenv.2018.09.032, URL https://www.sciencedirect.com/science/article/pii/S0360132318305900.

[16] R. McClung, H. Ge, J. Straube, J. Wang, Hygrothermal performance of cross-laminated timber wall assemblies with built-in moisture: field measurements and simulations, Build. Environ. 71 (2014) 95–110, http://dx.doi.org/10.1016/j.buildenv.2013.09.008, URL https://www.sciencedirect.com/science/article/pii/S0360132313002722.

[17] V. Kukk, J. Kers, T. Kalamees, L. Wang, H. Ge, Impact of built-in moisture on the design of hygrothermally safe cross-laminated timber external walls: A stochastic approach, Build. Environ. 226 (2022) 109736, http://dx.doi.org/10.1016/j.buildenv.2022.109736, URL https://www.sciencedirect.com/science/article/pii/S0360132322009660.

[18] V. Kukk, L. Kaljula, J. Kers, T. Kalamees, Designing highly insulated cross-laminated timber external walls in terms of hygrothermal performance: Field measurements and simulations, Build. Environ. 212 (2022) 108805, http://dx.doi.org/10.1016/j.buildenv.2022.108805, URL https://www.sciencedirect.com/science/article/pii/S0360132322000531.
[19] K. Kalbe, T. Kalamees, V. Kukk, A. Ruus, A. Annuk, Wetting circumstances, expected moisture content, and drying performance of CLT end-grain edges based on field measurements and laboratory analysis, Build. Environ. 221 (2022) 109245, http://dx.doi.org/10.1016/j.buildenv.2022.109245, URL https://www.sciencedirect.com/science/article/pii/S0360132322004802.
[20] E.L. Schmidt, M. Riggio, A.R. Barbosa, I. Mugabo, Environmental response of a CLT floor panel: Lessons for moisture management and monitoring of mass timber buildings, Build. Environ. 148 (2019) 609–622, http://dx.doi.org/10.1016/j.buildenv.2018.11.038, URL https://www.sciencedirect.com/science/article/pii/S0360132318307339.
[21] M. Autengruber, M. Lukacevic, J. F., Finite-element-based moisture transport model for wood including free water above the fiber saturation point, Int. J. Heat Mass Transfer 161 (2020) 120228, http://dx.doi.org/10.1016/j.ijheatmasstransfer.2020.120228, URL http://www.sciencedirect.com/science/article/pii/S0017931020331641.
[22] European Standard, EN ISO 15148:2003 Hygrothermal performance of building materials and products - Determination of water absorption coefficient by partial immersion, 2003.
[23] Y. Rodríguez Yon, L. Arias Pérez, A. Medina Carmona, Y. Mujica Pérez, L.R. Medina García, K. Fernández Suárez, A. Mena Echevarría, Alternative stainning technique to determine mycorrhizal colonization, Cultiv. Trop. 36 (2) (2015) 18–21, http://dx.doi.org/10.13140/RG.2.2.10232.65287, URL https://ediciones.inca.edu.cu.
[24] European Standard, EN 13183-2:2002 Moisture content of a piece of sawn timber Estimation by electrical resistance method, ISBN: 0 580 39691 6, 2002.
[25] K. Kalbe, A. Annuk, A. Ruus, T. Kalamees, Experimental analysis of moisture uptake and dry-out in CLT end-grain exposed to free water, J. Phys. Conf. Ser. 2069 (1) (2021) 012050, http://dx.doi.org/10.1088/1742-6596/2069/1/012050.
[26] J. Eitelberger, K. Hofstetter, S. Dvinskikh, A multi-scale approach for simulation of transient moisture transport processes in wood below the fiber saturation point, Compos. Sci. Technol. 71 (15) (2011) 1727–1738, URL http://www.sciencedirect.com/science/article/pii/S0266353811002946.
[27] S. Fortino, A. Genoese, A. Genoese, L. Nunes, P. Palma, Numerical modelling of the hygro-thermal response of timber bridges during their service life: A monitoring case-study, Constr. Build. Mater. 47 (2013) 1225–1234, URL http://www.sciencedirect.com/science/article/pii/S0950061813005278.
[28] S. Fortino, P. Hradil, A. Genoese, A. Genoese, A. Pousette, Numerical hygro-thermal analysis of coated wooden bridge members exposed to Northern European climates, Constr. Build. Mater. 208 (2019) 492–505, http://dx.doi.org/10.1016/j.conbuildmat.2019.03.012, URL https://www.sciencedirect.com/science/article/pii/S0950061819304854.
[29] H.L. Frandsen, L. Damkilde, S. Svensson, A revised multi-Fickian moisture transport model to describe non-Fickian effects in wood, Holzforschung 61 (2007) 563–572, URL http://www.degruyter.com/view/j/hfsg.2007.61.issue-5/hf.2007.085/hf.2007.085.xml.
[30] D. Konopka, M. Kaliske, Transient multi-Fickian hygro-mechanical analysis of wood, Comput. Struct. 197 (2018) 12–27, http://dx.doi.org/10.1016/j.compstruc.2017.11.012, URL https://www.sciencedirect.com/science/article/pii/S0045794917310684.
[31] K. Krabbenhøft, L. Damkilde, A model for non-fickian moisture transfer in wood, Mater. Struct. 37 (9) (2004) 615–622.
[32] K. Krabbenhøft, L. Damkilde, Double porosity models for the description of water infiltration in wood, Wood Sci. Technol. 38 (8) (2004) 641–659.
[33] Abaqus Documentation, Abaqus Online Documentation, Dassault Systemes Simulia Corporation, Providence, RI, USA, 2014.
[34] S. Avramidis, Evaluation of ‘‘three-variable’’ models for the prediction of equilibrium moisture content in wood, Wood Sci. Technol. 23 (3) (1989) 251–257, http://dx.doi.org/10.1007/BF00367738.
[35] C. Zuritz, R.P. Singh, S.M. Moini, S.M. Henderson, Desorption isotherms of rough rice from 10°C to 40°C, Trans. ASAE 22 (2) (1979) 0433–0436, http://dx.doi.org/10.13031/2013.35034, URL https://elibrary.asabe.org/abstract.asp?aid=35034.
[36] M. Autengruber, M. Lukacevic, C. Gröstlinger, J. Eberhardsteiner, J. Füssl, Numerical assessment of wood moisture content-based assignments to service classes in EC5 and a prediction concept for moisture-induced stresses solely using relative humidity data, Eng. Struct. 245 (2021) 112849, http://dx.doi.org/10.1016/j.engstruct.2021.112849, URL https://www.sciencedirect.com/science/article/pii/S0141029621009998.
[37] T. Volkmer, J.-A. Schmidt, K. Kranitz, P. Niemz, Untersuchungen zum Einfluss der Klebstoffart auf den Diffusionswiderstand von Holzverklebungen, Bauphysik 34 (2) (2012) 55–60, http://dx.doi.org/10.1002/bapi.201200006, arXiv:https://onlinelibrary.wiley.com/doi/pdf/10.1002/bapi.201200006 URL https://onlinelibrary.wiley.com/doi/abs/10.1002/bapi.201200006.
[38] D. Mannes, J.-A. Schmidt, P. Niemz, T. Volkmer, Untersuchungen zum Einfluss der Klebstoffart auf den kapillaren Wassertransport in Holz parallel zur Faserrichtung, Bauphysik 34 (2) (2012) 61–65.
[39] M. Lukacevic, M. Autengruber, T. Raimer, J. Eberhardsteiner, J. Füssl, Effect of cast-in-place concrete application on moisture distribution in timber-concrete composite floors with notched connections, investigated via finite element simulations, J. Build. Eng. 42 (2021) 103005, http://dx.doi.org/10.1016/j.jobe.2021.103005, URL https://www.sciencedirect.com/science/article/pii/S2352710221008639.
[40] H. Håkansson, Experimentiella studier av transient sorption i cellvägen i trä. Report TABK-94/3021, Tech. Rep., Lund Institute of Technology, Lund, Sweden, 1994.
[41] K. Sandberg, J.-G. Salin, Liquid water absorption in dried Norway spruce timber measured with CT scanning and viewed as a percolation process, Wood Sci. Technol. 46 (2012) 207–219, http://dx.doi.org/10.1007/s00226-010-0371-1.
[42] J. Johansson, G. Kifetew, CT-scanning and modelling of the capillary water uptake in Aspen, Oak and Pine, Eur. J. Wood Prod. 68 (1) (2010) 77–85, http://dx.doi.org/10.1007/s00107-009-0359-4.
[43] P. Perré, D.M. Nguyen, G. Almeida, A macroscopic Washburn approach of liquid imbibition in wood derived from X-ray tomography observations, Sci. Rep. 12 (1) (2022) 1750, http://dx.doi.org/10.1038/s41598-022-05508-0.
[44] L. Candanedo, D. Derome, Numerical simulation of water absorption in softwood, in: Ninth International IBPSA Conference, Montréal, Canada, 2005.
[45] G. AlSayegh, Hygrothermal Properties of Cross Laminated Timber and Moisture Response of Wood at High Relative Humidity, Carleton University, Ottawa, Ontario, 2012.
[46] S. Kordziel, S.V. Glass, C.R. Boardman, R.A. Munson, S.L. Zelinka, S. Pei, P.C. Tabares-Velasco, Hygrothermal characterization and modeling of cross-laminated timber in the building envelope, Build. Environ. 177 (2020) 106866, http://dx.doi.org/10.1016/j.buildenv.2020.106866.
[47] R.T.M. Lepage, Moisture Response of Wall Assemblies of Cross- Laminated Timber Construction in Cold Canadian Climates, University of Waterloo, Waterloo, Ontario, 2012.
[48] E.E. Thybring, M. Fredriksson, Wood and moisture, in: P. Niemz, A. Teischinger, D. Sandberg (Eds.), Springer Handbook of Wood Science and Technology, Springer International Publishing, Cham, 2023, pp. 355–397, http://dx.doi.org/10.1007/978-3-030-81315-4_7.
[49] C. Brischke, S.C. Lampen, Resistance based moisture content measurements on native, modified and preservative treated wood, Eur. J. Wood Wood Prod. 72 (2) (2014) 289–292, http://dx.doi.org/10.1007/s00107-013-0775-3, URL https://link.springer.com/article/10.1007/s00107-013-0775-3.
[50] M. Fredriksson, L.G. Thygesen, The states of water in Norway spruce (Picea abies (L.) Karst.) studied by low-field nuclear magnetic resonance (LFNMR) relaxometry: assignment of free-water populations based on quantitative wood anatomy, Holzforschung 71 (1) (2017) 77–90, http://dx.doi.org/10.1515/hf-2016-0044.
[51] K. Kalbe, V. Kukk, T. Kalamees, Identification and improvement of critical joints in CLT construction without weather protection, E3S Web Conf. 172 (2020) 10002, http://dx.doi.org/10.1051/e3sconf/202017210002.

[52] F. Brandstätter, M. Autengruber, M. Lukacevic, J. Füssl, Prediction of moisture-induced cracks in wooden cross sections using finite element simulations, Wood Sci. Technol. (2023) http://dx.doi.org/10.1007/s00226-023-01469-3.

[53] M. Lukacevic, W. Lederer, J. Füssl, A microstructure-based multisurface failure criterion for the description of brittle and ductile failure mechanisms of clear-wood, Eng. Fract. Mech. 176 (2017) 83–99, URL https://www.sciencedirect.com/science/article/pii/S0013794416307603.

[54] M. Lukacevic, J. Füssl, Application of a multisurface discrete crack model for clear wood taking into account the inherent microstructural characteristics of wood cells, Holzforschung 70 (9) (2016) 845–853, http://dx.doi.org/10.1515/hf-2015-0162.

[55] M. Lukacevic, J. Füssl, R. Lampert, Failure mechanisms of clear wood identified at wood cell level by an approach based on the extended finite element method, Eng. Fract. Mech. 144 (2015) 158–175, http://dx.doi.org/10.1016/j.engfracmech.2015.06.066, URL https://www.sciencedirect.com/science/article/pii/S001379441500332X.

[56] M. Li, J. Füssl, M. Lukacevic, J. Eberhardsteiner, C.M. Martin, Strength predictions of clear wood at multiple scales using numerical limit analysis approaches, Comput. I Struct. 196 (2018) 200–216, http://dx.doi.org/10.1016/j.compstruc.2017.11.005, URL https://www.sciencedirect.com/science/article/pii/S0045794917311550.

[57] M. Autengruber, M. Lukacevic, G. Wenighofer, R. Mauritz, J. Füssl, Finite-element-based concept to predict stiffness, strength, and failure of wood composite I-joist beams under various loads and climatic conditions, Eng. Struct. 245 (2021) 112908, http://dx.doi.org/10.1016/j.engstruct.2021.112908, URL https://www.sciencedirect.com/science/article/pii/S0141029621010567.